The Astrophysical Journal, 1004:117 (7pp), 2026 June 10 https://doi.org/10.3847/1538-4357/ae6e37

The Radio Emission from Radiative Filaments of the Cygnus Loop

D. Urošević[1], M. Andjelić[1], M. D. Filipović[2], Z. J. Smeaton[2], E. Crawford[2], J. Raymond[3], and D. Onić[1]
[1] Department of Astronomy, Faculty of Mathematics, University of Belgrade, Studentski trg 16, 11000 Belgrade, Serbia; dejanu@math.rs
[2] Western Sydney University, Locked Bag 1797, Penrith South DC, NSW 2751, Australia
[3] Center for Astrophysics | Harvard & Smithsonian, 60 Garden St., Cambridge, MA 02138, USA
Received 2026 March 3; revised 2026 May 11; accepted 2026 May 13; published 2026 June 9

Abstract

The Galactic supernova remnant (SNR) Cygnus Loop emerges as an ideal laboratory for analyzing the different radiation mechanisms, as well as the particle acceleration mechanisms at different types of shocks. In order to determine radio spectral indices of nonradiative and radiative filaments in the Cygnus Loop, we observed previously optically analyzed filaments with the Karl G. Jansky Very Large Array. At 1 and 5 GHz, we detected only radiative filaments in the field of view. Nonradiative optical filaments are also present but were not detected in radio. Instead of the expected nonthermal spectral slopes characteristic of SNRs, we observed spectral slopes characteristic of the thermal radiation mechanism from the radiative filaments in the Cygnus Loop. These evolutionary older parts of the Cygnus Loop radiate at radio frequencies predominantly via the thermal bremsstrahlung mechanism, and in that sense, their emission more closely resembles the radio emission of H II regions rather than the radio emission of SNRs.

Unified Astronomy Thesaurus concepts: Supernova remnants (1667); Shocks (2086); Interstellar medium (847)

1. Introduction

Shell-type supernova remnants (SNRs) are recognized as diffuse sources of radio continuum emission, predominantly through the synchrotron mechanism, both within the Milky Way and in several nearby galaxies (S. P. Reynolds et al. 2012; T. J. Galvin & M. D. Filipovic 2014; L. M. Bozzetto et al. 2017, 2023; P. Maggi et al. 2019; S. Ranasinghe & D. Leahy 2023; W. D. Cotton et al. 2024). Charged particles are accelerated at the shock waves via Fermi processes, making SNRs important sources of Galactic cosmic rays. There are other mechanisms of radiation contributing to the SNR continuum emission in the X- and γ-ray domains, as well as emission lines in the IR, optical and UV domains, which can be used to determine electron temperature, density, and other properties of disturbed matter by the SNR shock waves (see J. Vink 2012; M. D. Filipović & N. F. H. Tothill 2021 for more details). In addition, the radio continuum from evolved SNRs, especially those expanding in the high-density environments, can include a significant thermal bremsstrahlung component alongside the nonthermal synchrotron emission (D. Urošević & T. G. Pannuti 2005; D. Urošević et al. 2007; D. Onić et al. 2012; D. Onić 2013; D. Urošević 2014).

The dominant charged particle acceleration mechanism at SNR shocks is first-order Fermi acceleration, in particular, the so-called diffusive shock acceleration (DSA) process. In the test-particle limit for strong shocks with compression ratio $r = 4$, DSA predicts a particle energy spectrum $N(E) \propto E^{-2}$ and, consequently, a radio continuum synchrotron spectral index $\alpha \approx -0.5$, where the flux density $S_\nu \propto \nu^\alpha$ (W. I. Axford et al. 1977; G. F. Krymsky 1977; A. R. Bell 1978a, 1978b; R. D. Blandford & J. P. Ostriker 1978; R. D. Blandford & D. Eichler 1987). S. P. Reynolds (2011) discussed how nonlinear DSA can produce radio spectral indices that deviate from the canonical test-particle value and how that can be responsible for spectral flattening at higher radio continuum frequencies. However, the revised nonlinear DSA model that includes the so-called postcursor region implies spectra that are steeper than the standard DSA prediction (R. Diesing & D. Caprioli 2021). In addition, second-order Fermi (Fermi II) processes can also operate in the turbulent downstream regions and may be responsible for some observed values of integrated radio spectral indices of $\alpha \approx (-0.5, -0.3)$ (R. Schlickeiser & E. Fürst 1989; M. Ostrowski 1999).

SNR shocks can be classified into two types based on their evolutionary stage and shock velocity. During classical free expansion and Sedov–Taylor phases of evolution, so-called nonradiative shocks with high velocities (typically $>250\,\mathrm{km\,s^{-1}}$) efficiently accelerate particles to ultrarelativistic energies via the DSA process (see D. Urošević et al. 2019 and references therein). These electrons produce radio synchrotron emission, as well as X-ray synchrotron and γ-ray emission through inverse Compton or nonthermal bremsstrahlung processes (A. Tutone et al. 2021). In addition, cosmic-ray ions may be responsible for γ-ray emission through the so-called hadronic scenario via neutral pion decay (Y. Uchiyama et al. 2010). Nonradiative shocks can produce faint Hα emission by collisional excitation of neutral H atoms that pass through the shock. Because of the high temperatures, this can occur at low densities, and little radio bremsstrahlung is produced. On the other hand, for evolutionary older SNRs in post-Sedov–Taylor phases, with low shock velocities ($<250\,\mathrm{km\,s^{-1}}$), the shocks become radiative. That is, the shock heats the gas, but radiative cooling by the excitation of optical and UV spectral lines cools the gas to temperatures below 10^4 K. As the gas cools, it is compressed in order to maintain pressure equilibrium. DSA becomes more and more inefficient in these slower shocks. However, synchrotron radio emission may arise from adiabatic compression of preexisting cosmic-ray electrons and magnetic fields (van der Laan mechanism) or from particle reacceleration (H. van der Laan 1962; Y. Uchiyama et al. 2010; J. C. Raymond et al. 2020b;

D. Urošević 2022; M. D. Filipović et al. 2023, 2024). Bright Hα emission arises from the recombination in the gas that has cooled and become dense. It is accompanied by thermal bremsstrahlung (free–free) emission depending strongly on the square of the postshock electron number density n_e and only weakly on temperature T_e, with the volume emissivity scaling mainly as $\propto n_e^2 T_e^{-0.5}$, neglecting the slowly varying Gaunt factor for this purpose. In that sense, it is plausible that evolutionary older SNRs associated with high-density surroundings can exhibit both thermal bremsstrahlung and nonthermal synchrotron radio continuum emission (D. Onić et al. 2012). The corresponding radio spectral indices for thermal bremsstrahlung are between -0.1 and 2 ($\alpha = -0.1$ for the totally optically thin medium; $\alpha = 2$ for the totally optically thick medium).

Classification of SNRs as young, middle-aged, mature, and old is conventionally based on their estimated age and shock emission properties and evolutionary phase (J. K. Truelove & C. F. McKee 1999; J. Vink 2012; I. Chousein-Basia et al. 2026). However, the actual classical dynamical evolutionary stage (free expansion, Sedov–Taylor, and post-Sedov–Taylor) depends critically on both the real age as well as on the density and structure of the surrounding interstellar matter (ISM). For example, SNRs expanding through a low-density homogeneous ISM transition into subsequent evolutionary phases at much later times compared to those propagating through denser media. Of particular interest are remnants that expand through inhomogeneous environments or interact with molecular clouds, resulting in spatially varying local dynamical stages within the same object. Consequently, for many SNRs, including the Cygnus Loop, due to expansion through a complex, inhomogeneous environment, different parts of the same remnant can simultaneously be in different dynamical phases.

The Cygnus Loop (G74.0–8.5) is a well-known Galactic SNR, whose distance is estimated to be 725 ± 15 pc (R. A. Fesen et al. 2021) based on stellar parallaxes from the Gaia data, though A. M. Ritchey et al. (2024) showed that it may be as distant as 800 pc. It is a shell-type remnant without associated pulsar wind nebula. This middle-aged remnant (~20,000 yr old) has an angular diameter of ~3° on the sky. Its size and brightness make it suitable for studying smaller structures, e.g., filaments. J. C. Raymond et al. (2020a, 2020b) observed a portion of the western Cygnus Loop with the Hubble Space Telescope (HST) and a ground-based spectrograph. They were able to determine the preshock magnetic field and the compression ratio. By assuming that the preshock energetic electron and proton densities were the same as those measured outside our solar system by the Voyager satellites (A. C. Cummings et al. 2016), they predicted radio synchrotron and γ-ray hadronic pion emissivities based on the van der Laan mechanism in agreement with observations, though the filling factor of the emitting region remained a substantial uncertainty. Subsequently, A. Tutone et al. (2021) used better FERMI γ-ray maps and the reacceleration model of Y. Uchiyama et al. (2010) to separate the contributions of radiative and nonradiative regions within the Cygnus Loop. However, interpretation of the radio emission contains another uncertainty. The optically bright radiative shocks can also produce thermal bremsstrahlung radio emission, and the variations in spectral index around the Cygnus Loop (D.A. Green 1990) could result from varying ratios of thermal to nonthermal emission. The range in spectral index α among Green's 12 large regions was -0.56 to -0.23, which would suggest that some regions are dominated by thermal emission and others by nonthermal emission, if the spectra are optically thin. Much of the uncertainty in the interpretation of the radio emission stems from the low spatial resolution of the radio observations.

The Cygnus Loop SNR contains both nonradiative as well as radiative filaments. Different authors have measured the speeds of nonradiative filaments using different techniques (e.g., G. Salvesen et al. 2009; A. A. Medina et al. 2014). Recently, the speed of the shock wave has been determined by measuring the proper motions of both nonradiative and radiative filaments in the northeastern part of the Cygnus Loop (M. Vučetić et al. 2023). Radiative filaments are identified by their prominent [S II] emission, which arises from the cooled, dense postshock gas. M. Vučetić et al. (2023) confirmed that the radiative filaments in the northeastern rim of the Cygnus Loop remnant are detected in [S II] observations. As they are presumed to be evolutionarily older local parts, the expectation is that the radiative filaments should have lower expansion speeds in comparison to nonradiative ones. M. Vučetić et al. (2023) determined speeds of 39 nonradiative and three radiative filaments. The speeds obtained for the nonradiative filaments are in the range of 220–590 km s^{-1}, with uncertainties of 20–50 km s^{-1}, mostly in agreement with previous studies. The three radiative filaments (group of filaments labeled with H in M. Vučetić et al. 2023 and marked with a red ellipse in Figure 1) have significantly lower speeds of 110 ± 20 km s^{-1}. Given these particular velocity differences and the expected variation in particle acceleration efficiency or dominant emission mechanisms, differences in radio spectral indices between the two filament types are anticipated. High-resolution radio continuum observations can thus test whether particle acceleration (via DSA or reacceleration) operates in radiative shocks or if other processes, such as thermal bremsstrahlung, dominate. The Very Large Array (VLA) observations presented in this paper support the conclusion that synchrotron emission is not the dominant mechanism in the radiative filaments of the northeastern rim of the Cygnus Loop remnant.

2. VLA Observations

As the Cygnus Loop's filaments are often only several arcseconds across, obtaining their radio spectral indices demands observations with sufficiently high resolution. Therefore, we obtained observations with VLA in both B and C configurations, at 1 GHz (*L* band; 1.008–2.032 GHz; total 1.024 GHz bandwidth) and 5 GHz (*C* band; 4.743–6.511 GHz; total 1.768 GHz bandwidth) (project 24A-190, PI: D. Uroševic). The size of the field of view (FOV) at 1 GHz was large enough to cover both radiative and nonradiative filaments with one pointing (see Figure 1), while we observed two FOVs at 5 GHz, each covering radiative and nonradiative filaments, as proposed by optical observations (M. Vučetić et al. 2023). Nonradiative filaments observed with VLA are marked with blue dashed-line ellipses (groups of filaments labeled with F and K in M. Vučetić et al. 2023), while the three radiative filaments are marked with a red dashed-line ellipse in Figure 1 (labeled with H in M. Vučetić et al. 2023).

We have obtained ~40 hr of observations with the VLA of NRAO[4] in the B and C array configurations. C array observations were done from 2024 March 25–2024 April 19 (15 hr), and B array observations were done from 2024 August

[4] The National Radio Astronomy Observatory is a facility of the National Science Foundation operated under cooperative agreement by Associated Universities, Inc.

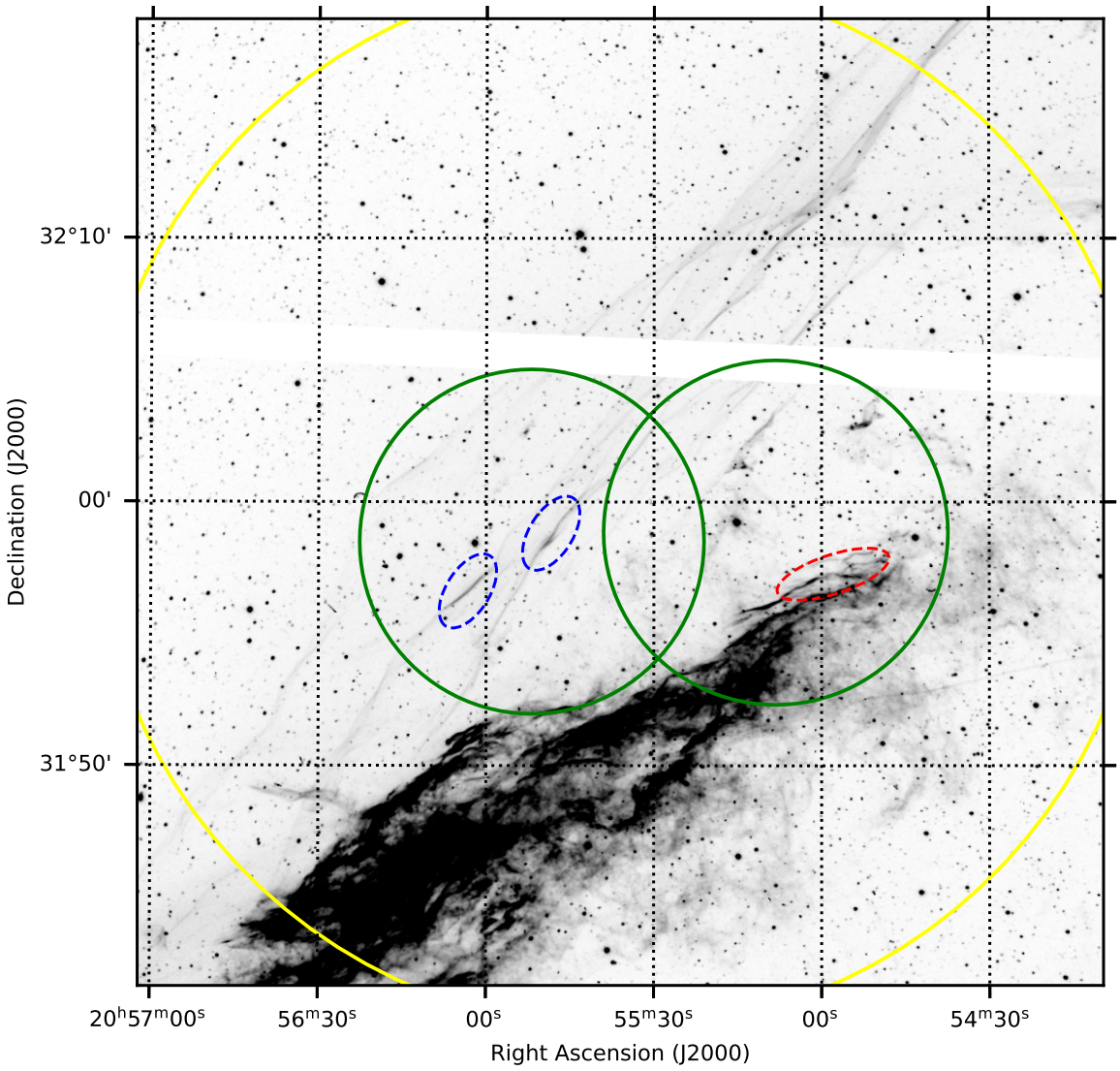

Figure 1. Context of our observations. The background image shows Hα emission (from 1993) of the northeastern part of Cygnus Loop (courtesy of R. Fesen). Yellow and green circles mark VLA pointing (primary beams) at 1 and 5 GHz. Two fields of view at 5 GHz were needed in order to cover both nonradiative filaments (blue dashed-line ellipses), labeled with F and K in M. Vučetić et al. (2023), and radiative filaments (red dashed-line ellipse), labeled with H in M. Vučetić et al. (2023).

16–September 3 (25 hr). Each of these observations were split into ∼100 minute blocks, each consisting of pointings to the phase calibrator (J2052+3635), flux calibrator (3C286), and six 12 minute exposures out of 12 minutes on the target (filament). Total exposure time on filaments at 1 GHz was 7.2 hr, while we had a total of 10.8 hr at 5 GHz. There are previous VLA observations that cover the same filaments observed here (W. C. Straka et al. 1986) at 17.8 cm (∼1.7 GHz). However, due to the significantly smaller bandwidth of the older observations (37.5 MHz total) their addition is not likely to substantially improve the sensitivity of our combined 1 GHz image, and the data were therefore not incorporated.

The data reduction was performed with the science pipeline version 2025.1.0.32 (B. R. Kent et al. 2020)[5] following the heuristics embedded in the pipeline. The measurement sets were presented to the pipeline, jointly deconvolved and self-calibrated with models derived from the combined dataset. Imaging was performed using the CASA TCLEAN function with Briggs weighting (robust = 0.5), multifrequency synthesis deconvolution (convolver = mtmfs, nterms = 2), and a standard gridder with no tapering applied. The finer-than-nominal angular resolution of $4\farcs3 \times 3\farcs6$ (position angle - P.A. $= -84°$) for 1 GHz and $1\farcs6 \times 1\farcs4$ (P.A. $= -69°$) for 5 GHz results from the use of robust = 0.5 weighting, which upweights the longer baselines relative to naturally weighted data. This process resulted in the final 1 and 5 GHz high-resolution images (see Figure 2).

The local noise level was measured in background regions and is around 6 μJy beam^{-1} for the 1 GHz image and 2 μJy beam^{-1} for the 5 GHz image. The average rms in the residual images is reported from the pipeline as 5.6 μJy beam^{-1} for 1 GHz and 1.5 μJy beam^{-1} for 5 GHz. These values closely match the measured background noise values, indicating that the imaging is well converged with no significant undeconvolved flux remaining.

[5] Details of the pipeline can be found on the NRAO website: https://science.nrao.edu/facilities/vla/data-processing/pipeline.

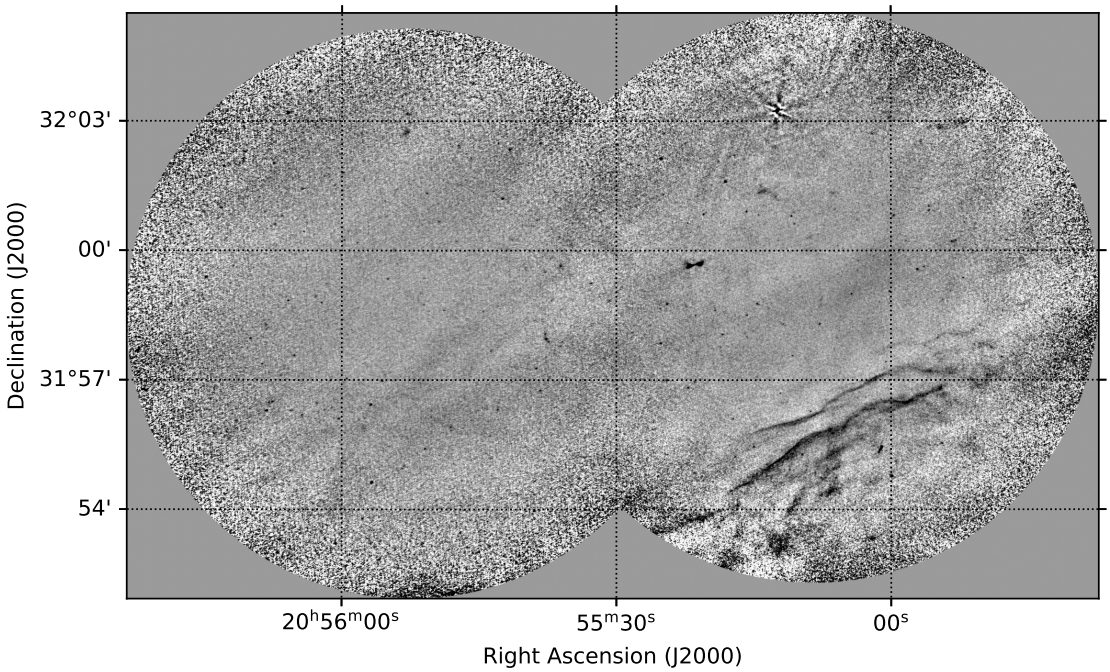

Figure 2. VLA combined B- and-C-array image of the northeastern part of the Cygnus Loop at 5 GHz. Radiative filaments H are visible in the lower right. Nonradiative filaments F and K, visible in optical emission lines (Figure 1), are not detected in radio.

3. Results and Discussion

In Figure 2 we present our image obtained at 5 GHz. From visual inspection, it can be seen that nonradiative filaments F and K are not detected, while the radiative ones are clearly visible. The same conclusion stands also for VLA observations at 1 GHz. We also checked the lower-resolution image—C array at 1 GHz, for possible detection of nonradiative filaments—but without success.

As already noted—we use nomenclature for filaments introduced in M. Vučetić et al. (2023). In this work, localized group of filaments that was visible in ionized sulfur lines, with measured shock velocities of $\simeq$110 km s^{-1}, and hence taken as in radiative phase, were labeled with H1, H2, and H3. The method for measuring shock speeds in M. Vučetić et al. (2023) was suitable only for nearly linear segments of filaments. Therefore, this region has much more filaments, or segments of filaments, which are visible in radio, as well as in optical emission. This is why we introduced additional labeling for filaments in this region: H1-a, which continues on H1, and H4 (see bottom left panel of Figure 3). Emission visible at the bottom left part of the 1 GHz VLA image (see Figure 3, top left panel), which slightly extends on the H4 filament, and shows steeper spectral index ($\alpha < -0.3$) is not labeled as it is not taken into consideration in the discussion. This segment is on the edge of the VLA field, which strongly affects spectral index measurement, and hence, it is unreliable. In addition to this, the region near the southern edge of 1 GHz image is rather complex and not filament-like, as can be seen from optical radiation (Figure 3, top right panel), so it could be that the foreground or background emission is contaminating filament radiation and affecting the spectral index estimate.

The first impression to take into account when trying to explain why we failed to detect the F and K nonradiative filaments is that they are thinner in their spatial extensions in Hα compared to radiative filament H (Figure 1) and of lower optical brightness. To roughly estimate the 3σ upper limits on the integrated flux densities, we note again that the local rms noise level $\sigma_{\rm rms}$ (the continuum noise per beam), measured in source-free background regions, is $\sim$5.6 μJy beam^{-1} at 1 GHz and $\sim$1.5 μJy beam^{-1} at 5 GHz. The beam area for the Gaussian synthesized beam is 17.54 arcsec^2 and 2.54 arcsec^2, at 1 GHz and 5 GHz, respectively. The angular extent of the brightest and largest nonradiative filament F, as seen in Hα, is around $\sim$5″–15″ wide and $\sim$140″ long (M. Vučetić et al. 2023). Let the filament area be $700 - 2100$ arcsec^2. The number of synthesized beams covered by the filament, i.e., the filament area divided by the effective beam area, is $N_{\rm beams}$. Nonradiative filaments cover an area corresponding to roughly $N_{\rm beams} = 40$–276 beams at 1 GHz and $N_{\rm beams} = 120$–827 beams at 5 GHz, depending on the exact width and length of each filament. The estimated 3σ upper limits on the integrated flux density were therefore calculated in the standard way for extended sources as $3\sigma_{\rm rms} \times \sqrt{N_{\rm beams}}$ (A. E. Sansom et al. 2019) and amount to $\lesssim$106–279 μJy at 1 GHz and $\lesssim$49–129 μJy at 5 GHz, as the exact value depends on the precise area of each filament. These upper limits are lower than the measured flux densities of the radiative filaments H1, H1-a, and H4 ($\sim$0.9–5.6 mJy at 1 GHz; see Table 1). However, the low radio brightness is expected theoretically for nonradiative shocks expanding into lower-density ISM ($\sim$0.2–1.5 cm^{-3}) with higher shock velocities ($\sim$220–590 km s^{-1}), in contrast to the higher postshock densities ($\sim$6 cm^{-3}) of the radiative filaments (J. C. Raymond et al. 2020b; A. Tutone et al. 2021). The brightness of Hα emission depends on the square of postshock number density. On the other hand, the synchrotron emissivity depends only linearly on postshock density (A. R. Bell 1978b). The nonradiative filaments, detected in Hα, emit radio synchrotron radiation (D. Urošević et al. 2019). Furthermore, the radio emission from nonradiative filaments will drop down under the sensitivity limit (in B and C configurations of VLA at 1 GHz, and especially at 5 GHz), much faster than Hα emission. This is consistent with the previous modeling of the Cygnus

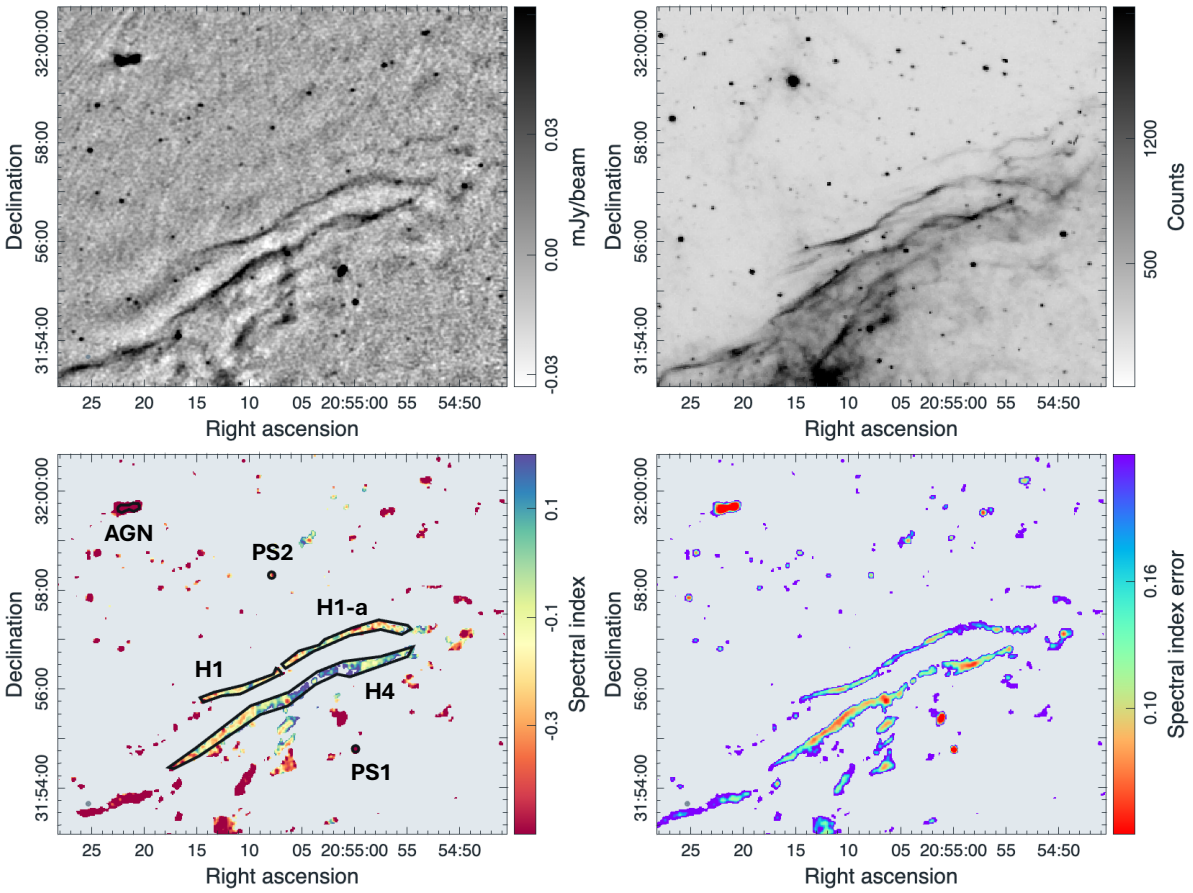

Figure 3. 1 GHz VLA radio continuum (top left), optical Hα image (top right), spectral index map generated from VLA 1 and 5 GHz observations (bottom left), and associated spectral index error map (bottom right) zoomed in on filaments of interest. Radiative filaments are divided into H1, H1-a, and H4 regions. AGN and two point sources (PS1 and PS2) are also marked. The spectral index image (bottom left) is scaled between −0.5 and 0.2 to show the filament variation. Therefore, the lower end of the color bar is becoming saturated at the low end for steep spectrum sources.

Loop (J. C. Raymond et al. 2020a; A. Tutone et al. 2021), which predicts a significantly lower synchrotron surface brightness in the nonradiative regions due to their lower postshock densities.

The spectral index map was generated by convolving the 1 and 5 GHz VLA images to a common beam size of 5″ and then calculating the spectral index as the linear fit of two points in log–log space using the MIRIADMATHS function (see Figure 3, bottom left). We also generated a spectral index error map with the same resolution following standard error propagation. This error map was used to estimate the average uncertainties reported in Table 1. We marked three regions around the filaments (labeled H1, H1-a, and H4), two background point sources (PS1 and PS2), and one background active galactic nucleus (AGN) (see Figure 3, bottom left and Table 1). The spectral index uncertainties reported in Table 1 are the average values from the spectral index map using the same region. For the filament regions, we also report the standard deviation of the values from the spectral index map (shown as the bracketed values in Table 1, column (4)), which effectively represent the variation in the spectral index value over the filament. This is a representation of how accurate the reported average value is for the entire filament, as the filaments are sufficiently large that there is spectral variation present. This background AGN is the Parkes-MIT-NRAO (PMN) source NVSS J205521+315942 (J. J. Condon et al. 1998), but it was not reported as an AGN. This was likely due to the lower resolution of PMN, and in our VLA image, it appears as a clear AGN double-lobed structure. To validate the spectral index map, we measure the flux densities of these regions individually, assuming a 10% uncertainty following the same procedure as outlined in M. D. Filipović et al. (2022, 2025). This 10% uncertainty is a conservative estimate, which includes the nominal 3%–5% flux calibration accuracy of VLA, as well as additional contributions from residual calibration and imaging uncertainties. We use flux measurements of these sources to calculate the spectral index independently to compare them with the average values from the spectral index map (see Table 1). We find that the manually calculated spectral indices match closely with the values obtained from the map for all points except for one of the point sources (PS2). This discrepancy is likely due to the faintness of this point source and so does not hinder the accuracy of the filament measurements, which are at least an order of magnitude brighter. The manual measurements for the filaments are consistent with those from the map, providing confidence in our measurements. The PS1, PS2, and AGN spectral indices are typical for their source type as background point sources and AGN (M. D. Filipović & N. F. H. Tothill 2021), providing further justification.

The spectral index map between 1 and 5 GHz, presented in Figure 3 bottom left, shows slight differences between the northern (H1 and H1-a parts) and southern (H4 part) radiative filaments. The southern filament shows, on average, a higher spectral index value than the northern filament. The values for

Table 1
Spectral Indices and Flux Density Measurements of Different Regions in the FOV

Region	$S_{1\ \mathrm{GHz}} \pm \Delta S_{1\ \mathrm{GHz}}$ (mJy)	$S_{5\ \mathrm{GHz}} \pm \Delta S_{5\ \mathrm{GHz}}$ (mJy)	$\alpha \pm \Delta\alpha$ (Map)	α (Flux Densities)
H1-a	1.4 ± 0.1	1.1 ± 0.1	-0.19 ± 0.19 (0.26)	–0.16
H1	0.9 ± 0.1	0.7 ± 0.1	-0.17 ± 0.17 (0.24)	–0.16
H4	5.6 ± 0.6	5.5 ± 0.6	-0.03 ± 0.14 (0.19)	–0.02
PS1	0.6 ± 0.1	0.26 ± 0.03	-0.54 ± 0.04	–0.56
PS2	0.06 ± 0.01	0.05 ± 0.01	-0.39 ± 0.16	–0.11
AGN	5.9 ± 0.6	1.7 ± 0.2	-0.79 ± 0.02	–0.78

Note. The flux density measurements assume an overall error of 10%. The spectral index is calculated separately from the spectral index map (column (4)) and also from the flux density measurements (column (5)) for validation. The spectral index uncertainties given in column (4) are taken as the average values from the spectral index error map, and the bracketed values show the standard deviation of the values in each region, reflecting the variation in the filament values.

these filaments are around $\alpha = 0$ and $\alpha = -0.2$, respectively. Although the intervals of spectral index for the northern and southern filaments, given the large uncertainty, overlap, we interpret possible reasons for the differences. The variation in spectral index values between these two filaments could be caused by differences in the densities of the medium in both filaments. If the density of the medium is higher, the optical thickness of the medium will be higher, and it converges to the higher spectral indices of thermal bremsstrahlung emission (in the frequency region where the thermal bremsstrahlung spectra takes a break, for which the optical depth τ takes values around 1). In the limit of the totally optically thick medium, for which the optical depth $\tau \gg 1$, the radio spectral index tends to a blackbody radiation value of $\alpha = 2$. The values for the spectral indices of our two filaments (southern and northern) approximately correspond to a totally thin medium where $\tau \ll 1$ and so $\alpha = -0.1$. At the end, the southern filament could be at a slightly higher-average, medium density than the northern one and therefore would have a higher spectral index of thermal bremsstrahlung emission. Looking at the spectral index of the H1 and H4 filaments in the lower-resolution data of D. A. Green (1990, their region C), we see that they obtained a steeper spectral index of -0.35. That might indicate a mixture of thermal and nonthermal emission in this part of the Cygnus Loop. If so, it is plausible that bright optical filaments would be dominated by thermal emission, while the nonthermal emission could be more diffuse and therefore make a larger fractional contribution to the low-resolution observation. It is also possible that the bright optical filaments, being sheets of emitting gas seen edge-on (J. J. Hester 1987) could be optically thick, while the optically fainter, but more extended, regions surrounding the filaments, would be optically thin.

J. C. Raymond et al. (2020a, 2020b) and A. Tutone et al. (2021) showed that the van der Laan mechanism or cosmic-ray reacceleration could match the radio surface brightness and the γ-ray emission from the radiative shock regions of the Cygnus Loop. The detection of γ-rays from the radiative shock regions of the Cygnus Loop (A. Tutone et al. 2021) indicates that energetic protons are interacting with the dense postshock gas. That means that particle acceleration by the van der Laan mechanism or reacceleration does really occur, even if thermal bremsstrahlung dominates in the radio. We have shown that much of the radio continuum emission from these regions is thermal bremsstrahlung rather than synchrotron emission. The conclusions of those studies regarding the γ-ray luminosity are unchanged, but the synchrotron emission that they aimed to explain is brighter than is actually observed. Given the uncertainties in the filling factor and the preshock cosmic-ray electron population, and assuming that the magnetic field strength and compression ratio derived for a small area can be applied to much larger regions, their conclusion that DSA acceleration is not needed to explain the radio synchrotron emission still holds. However, our work highlights uncertainties in comparing predicted and observed nonthermal radio fluxes, so a stronger conclusion that DSA is negligible would not be warranted.

While the measured radio spectral indices for the radiative filaments for the northern parts H1 and H1-a, and for the southern part H4, are significantly flatter than the canonical synchrotron value of $\alpha \approx -0.5$ predicted by test-particle DSA for strong shocks, these values are fully consistent with thermal bremsstrahlung emission in the optically thin limit. The uncertainties on the spectral indices derived from the map and the standard deviation of the values within each filament region (see Table 1) mean that the data cannot completely rule out a small synchrotron contribution. However, the central values and the nondetection of the nonradiative filaments F and K strongly favor thermal bremsstrahlung as the dominant mechanism in the dense, radiative postshock gas.

K. W. Weiler et al. (1986, 1989, 2009) showed that radio emission from supernovae and young remnants frequently exhibits spectral flattening or curvature due to free–free absorption, environmental effects, and time-dependent optical depth changes. These effects are also relevant for evolutionary older SNRs expanding in dense and highly heterogeneous environments. Similarly, G. Dubner & E. Giacani (2015) emphasized the difficulties in interpreting radio spectra of evolved SNRs, where mixed thermal and nonthermal emission, incomplete frequency sampling, and limited spatial resolution often lead to apparent deviations from pure synchrotron behavior. In the specific case of the radiative shocks in the Cygnus Loop, the high postshock densities naturally enhance the thermal bremsstrahlung contribution, making it the dominant radio continuum mechanism despite the presence of cosmic-ray electrons.

We note the results of M. Arias et al. (2019) for the mixed-morphology SNR VRO 42.05.01, which displays a relatively flat radio spectral index at higher radio continuum frequencies ($\alpha \approx -0.37$), together with curvature that leads to spectral steepening at low frequencies (as probed by LOFAR at 143 MHz). They emphasized that the observed curvature in the low-frequency end of the radio spectrum occurs primarily in the brightest regions of the source, while the fainter regions present a roughly constant power-law behavior between 143 and 2695 MHz. The authors favor an explanation in which

radiative shocks possess high compression ratios ($\chi > 4$), such that electrons of different energies scatter over different length scales in the postshock region and therefore sample varying effective compression ratios. Lower-energy electrons (corresponding to lower radio frequencies) probe regions closer to the shock front with lower compression, resulting in steeper local spectral indices. While the Cygnus Loop radiative filaments also exhibit flat spectral indices associated with radiative shocks, our interpretation at 1–5 GHz differs. The observed values are much more consistent with the optically thin thermal bremsstrahlung limit ($\alpha \approx -0.1$), and the nondetection of the nonradiative filaments F and K (which would be expected to be synchrotron bright if, e.g., DSA, Fermi II, or reacceleration were dominant) versus the clear detection of the radiative filament H strongly favors thermal bremsstrahlung as the dominant emission mechanism. The high-compression-ratio synchrotron scenario proposed by M. Arias et al. (2019) would still predict nonthermal emission, but the brightness contrast and the measured spectral indices in our VLA data support thermal dominance at these frequencies. Low-frequency observations with greater sensitivity would be needed to test whether similar curvature effects are present in the radiative shocks of the Cygnus Loop.

4. Summary

In this paper, we present new VLA observations at 1 and 5 GHz of the selected filaments in the northeastern rim of Cygnus Loop in order to determine the radio spectral indices of nonradiative and radiative filaments previously observed in the optical range. In the observed FOVs, there are no detections of the nonradiative filaments, while the radiative filaments are clearly visible. Contrary to expected synchrotron spectral slopes of around −0.5, characteristic for shell-type SNRs, the observed shallower values of radio spectral indices for the radiative filaments in the Cygnus Loop indicate that the thermal bremsstrahlung is the dominant radiation mechanism for the production of their radio continuum emission.

Acknowledgments

We thank the reviewer for comprehensive suggestions that significantly improved this article. D.U., M.A., and D.O. are supported by the Ministry of Science, Technological Development and Innovation of the Republic of Serbia, through contract No. 451-03-33/2026-03/200104. D.U. and M.A. are also supported through the joint project of the Serbian Academy of Sciences and Arts and Bulgarian Academy of Sciences—"Detection and Kinematic Characterization of Optical Counterparts to Radio Supernova Remnants."

ORCID iDs

D. Urošević https://orcid.org/0000-0003-0665-0939
M. Andjelić https://orcid.org/0000-0003-3146-234X
M. D. Filipović https://orcid.org/0000-0002-4990-9288
Z. J. Smeaton https://orcid.org/0009-0009-7061-0553
E. Crawford https://orcid.org/0000-0001-5197-1091
J. Raymond https://orcid.org/0000-0002-7868-1622
D. Onić https://orcid.org/0000-0002-2130-2011

References

Arias, M., Vink, J., Iacobelli, M., et al. 2019, A&A, 622, 6
Axford, W. I., Leer, E., & Skadron, G. 1977, ICRC, 11, 132
Bell, A. R. 1978a, MNRAS, 182, 147
Bell, A. R. 1978b, MNRAS, 182, 443
Blandford, R. D., & Eichler, D. 1987, PhR, 154, 1
Blandford, R. D., & Ostriker, J. P. 1978, ApJ, 221, 29
Bozzetto, L. M., Filipović, M. D., Sano, H., et al. 2023, MNRAS, 518, 2574
Bozzetto, L. M., Filipović, M. D., Vukotić, B., et al. 2017, ApJS, 230, 2
Chousein-Basia, I., Zezas, A., Leonidaki, I., & Kopsacheili, M. 2026, MNRAS, 545, staf1819
Condon, J. J., Cotton, W. D., Greisen, E. W., et al. 1998, AJ, 115, 5
Cotton, W. D., Filipović, M. D., Camilo, F., et al. 2024, MNRAS, 529, 2443
Cummings, A.C., Stone, E.C., Heikkila, B.C., et al. 2016, ApJ, 831, 18
Diesing, R., & Caprioli, D. 2021, ApJ, 922, 1
Dubner, G., & Giacani, E. 2015, A&ARv, 23, 3
Fesen, R. A., Weil, K. E., Cisneros, I., et al. 2021, MNRAS, 507, 244
Filipović, M. D., Dai, S., Arbutina, B., et al. 2023, AJ, 166, 149
Filipović, M. D., Lazarević, S., Araya, M., et al. 2024, PASA, 41, e112
Filipović, M. D., Payne, J. L., Alsaberi, R. Z. E., et al. 2022, MNRAS, 512, 265
Filipović, M. D., Smeaton, Z. J., Kothes, R., et al. 2025, PASA, 42, e104
Filipović, M. D., & Tothill, N. F. H. 2021, Multimessenger Astronomy in Practice (IOP Publishing)
Galvin, T. J., & Filipović, M. D. 2014, SerAJ, 189, 15
Green, D.A. 1990, AJ, 100, 1927
Hester, J.J. 1987, ApJ, 314, 187
Kent, B. R., Masters, J. S., Chandler, C. J., et al. 2020, ASPC, 527, 571
Krymsky, G. F. 1977, DoSSR, 234, 1306
Maggi, P., Filipović, M. D., Vukotić, B., et al. 2019, A&A, 631, A127
Medina, A. A., Raymond, J. C., Edgar, R. J., et al. 2014, ApJ, 791, 30
Onić, D. 2013, Ap&SS, 346, 3
Onić, D., Urošević, D., Arbutina, B., & Leahy, D. 2012, ApJ, 756, 61
Ostrowski, M. 1999, A&A, 345, 256
Ranasinghe, S., & Leahy, D. 2023, ApJS, 265, 53
Raymond, J. C., Chilingarian, I. V., Blair, W. P., et al. 2020a, ApJ, 894, 108
Raymond, J. C., Slavin, J. D., Blair, W. P., et al. 2020b, ApJ, 903, 2
Reynolds, S. P. 2011, Ap&SS, 336, 257
Reynolds, S. P., Gaensler, B. M., & Bocchino, F. 2012, SSRv, 166, 231
Ritchey, A. M., Federman, S. R., & Lambert, D. L. 2024, MNRAS, 528, 4490
Salvesen, G., Raymond, J. C., & Edgar, R. J. 2009, ApJ, 702, 327
Sansom, A. E., Glass, D. H. W., Bendo, G. J., et al. 2019, MNRAS, 482, 4617
Schlickeiser, R., & Fürst, E. 1989, A&A, 219, 192
Straka, W. C., Dickel, J. R., Blair, W. P., et al. 1986, ApJ, 306, 266
Truelove, J. K., & McKee, C. F. 1999, ApJS, 120, 299
Tutone, A., Ballet, J., Acero, F., et al. 2021, A&A, 656, A139
Uchiyama, Y., Blandford, R. D., Funk, S., et al. 2010, ApJL, 723, L122
Urošević, D. 2014, Ap&SS, 354, 541
Urošević, D. 2022, PASP, 134, 061001
Urošević, D., Arbutina, B., & Onić, D. 2019, Ap&SS, 364, 185
Urošević, D., & Pannuti, T. G. 2005, APh, 23, 577
Urošević, D., Pannuti, T. G., & Leahy, D. 2007, ApJL, 655, L41
van der Laan, H. 1962, MNRAS, 124, 179
Vink, J. 2012, A&ARv, 20, 49
Vučetić, M., Milanović, N., Urošević, D., et al. 2023, SerAJ, 207, 9
Weiler, K. W., Panagia, N., Sramek, R. A., et al. 1989, ApJ, 336, 421
Weiler, K. W., Panagia, N., Sramek, R. A., et al. 2009, AIPC, 1111, 440
Weiler, K. W., Sramek, R. A., Panagia, N., van der Hulst, J. M., & Salvati, M. 1986, ApJ, 301, 790